processes

MDPI

Article

Pressure Relief-Type Overpressure Distribution Prediction Model Based on Seepage and Stress Coupling

Gaolong Liao [1,*], Shusheng Guo [1], Chao Wang [1], Yuan Shen [1] and Yanfang Gao [2,*]

[1] CNOOC (China) Co., Ltd., Hainan Branch, Haikou 570312, China
[2] Department of Geology, Northwest University, Xi'an 710069, China
* Correspondence: liaogl2@cnooc.com.cn (G.L.); gaoyanfang@nwu.edu.cn (Y.G.)

Abstract: At present, great progress has been made in the prediction of undercompaction and fluid expansion overpressure. However, in recent years, the field has frequently encountered pressure relief-type overpressure. Different from primary overpressure, such as undercompaction and fluid expansion, this type of overpressure belongs to secondary overpressure, which has a certain concealment in response to seismic velocity and logging data. Based on this, a geological analysis model of pressure relief-type overpressure was established according to the seepage and stress coupling theory. The model can realize the prediction of pressure relief range and pressure distribution, which provides a new way to predict this kind of overpressure. The influence of the laws of porosity, permeability, and geological movement on pressure relief were analyzed. The research results provide a new method for the prediction of pressure relief-type overpressure and improving the basic guarantee of safe and efficient drilling.

Keywords: pressure relief; overpressure; seepage

check for updates

Citation: Liao, G.; Guo, S.; Wang, C.; Shen, Y.; Gao, Y. Pressure Relief-Type Overpressure Distribution Prediction Model Based on Seepage and Stress Coupling. *Processes* **2023**, *11*, 480. https://doi.org/10.3390/pr11020480

Academic Editors: Chuanliang Yan, Kai Zhao, Fucheng Deng and Yang Li

Received: 24 December 2022
Revised: 30 January 2023
Accepted: 2 February 2023
Published: 5 February 2023

Copyright: © 2023 by the authors. Licensee MDPI, Basel, Switzerland. This article is an open access article distributed under the terms and conditions of the Creative Commons Attribution (CC BY) license (https://creativecommons.org/licenses/by/4.0/).

1. Introduction

Formation pore pressure refers to the pressure of fluid (oil, gas, water) in the pores of rocks, also known as pore pressure or formation pressure. Normal pore pressure is equal to hydrostatic pressure from the continuous formation water from the surface to somewhere underground. Pore pressure higher than hydrostatic pressure is called abnormally high pressure. In drilling engineering, accurate determination of pore pressure is conducive to a reasonable selection of drilling fluid density and scientific design of the casing program, which can not only realize efficient and safe drilling but also protect the reservoir to the greatest extent.

There are a variety of pressure-forming mechanisms for abnormally high pressures. Swarbrick [1] classified the pore pressure formation mechanisms into three categories, including porosity reduction due to stress (including undercompaction and tectonic compression), fluid volume expansion (including hydrothermal pressurization, hydrocarbon generation, and mineral conversion), and fluid transport and buoyancy (including fluid transport, osmosis, water head, and buoyancy). It is pointed out that fluid migration in the same inclined reservoir or between different reservoirs may affect the identification of abnormal pressure formation mechanisms. Bowers [2] classified abnormally high pressure formation mechanisms into four categories, including undercompaction, fluid expansion (including hydrothermal pressurization, hydrocarbon generation, and mineral transformation), fluid migration, and tectonic compression. It is particularly emphasized that it is difficult to identify fluid migration and tectonic compression from well logging data, which should be combined with the history of tectonic movement. Ozkale [3] classified abnormally high pressure formation mechanisms into four categories, including undercompaction, fluid volume expansion (including hydrothermal pressurization, hydrocarbon generation, and mineral transformation), fluid migration and buoyancy (including fluid

migration, osmosis, water head, and buoyancy), and tectonic movement (fluid migration caused by tectonic compression, tectonic shear, and reverse faults). Fan [4] classified abnormally high pressure formation mechanisms into four categories according to the mechanical relationship in the sedimentary process of shale. They include those consistent with the original sedimentary loading mechanism (undercompaction), those consistent with the reloading mechanism (including tectonic extrusion, diapir, and faulting), those consistent with the unloading mechanism (including mineral transformation [5], fluid transport, hydrothermal pressurization, osmosis, hydrocarbon generation, and formation uplift), and those consistent with basically unchanged porosity (buoyancy).

The accurate determination of the formation mechanism of overpressure is key for the accurate calculation of pore pressure. Bowers [6] found in his study that the logging data of formations with undercompaction and fluid expansion (including hydrothermal pressurization, hydrocarbon generation, fluid migration, and mineral conversion) were different. The relationship between acoustic velocity and effective stress in underpressurized strata was consistent with the loading mechanism, while the relationship between acoustic velocity and effective stress in fluid expansion strata was consistent with the unloading mechanism. This is because acoustic velocity and resistivity are more sensitive than porosity and formation density during unloading. This study provided a good basis for identifying the mechanism of abnormal pressure formation. Bowers [7] proposed that the intersection of the sonic time difference and formation density can clearly reflect the normal trends of decreasing and increasing sonic time difference and formation density with formation compaction, respectively. The sonic time difference and density of formation with abnormally high pressure caused by undercompaction (loading) are above this normal trend. However, in strata with abnormally high pressure caused by fluid expansion (unloading), the sonic time difference and density will deviate from this trend, showing a phenomenon of high sonic time difference but basically unchanged density. Bowers [2] also proposed a simple way to distinguish between undercompaction and fluid expansion. If the acoustic time difference, resistivity, and density at the same depth of the anomaly were extended vertically upward at the same time to intersect the log line, and if all three intersects were still at the same depth, the abnormally high pressure was due to undercompaction. If the density intersection was lower than the other two, this meant the abnormally high pressure was caused by fluid expansion. Stephen et al.'s [8] research found that in the process of mineral conversion or hydrocarbon generation, the porosity of the rock skeleton, rock pore destruction, and the change of skeleton cement will affect the sonic time difference and rock density. If the formation was not completely enclosed, the formation density would increase and the sound velocity would decrease.

Different pore pressure evaluation methods have been established for abnormally high pressures with different formation mechanisms [9–12]. Eaton [13] proposed the Eaton model for determining pore pressure using resistivity, conductivity, index, and sonic time difference. This model has been widely used in predicting and monitoring abnormally high pressure caused by undercompaction of mudstone. However, the determination of the normal trend line and empirical parameters in this method is highly subjective, which has great influence on the calculation results, and this problem has not been effectively solved. Zhang [14] modified the Eaton method according to the relationship between porosity and effective stress, taking the logarithmic difference of the acoustic time difference as the index to determine pore pressure, which strengthened the theoretical basis of the method. However, this method can only be used to determine abnormally high pressure caused by undercompaction. Khaksar [15] analyzed the applicability of the conventional acoustic-effective stress relationship for the determination of pore pressure, indicating that the factors affecting the acoustic velocity of rocks include stress, porosity, lithology, fluid properties, and pore shape. Yu et al.'s [16] study on the abnormally high pressure of the continental shelf of the Gulf of Mexico showed that the S-wave velocity was more sensitive to the abnormally high pressure than the P-wave velocity. Therefore, the P-wave ratio could be used to replace the P-wave velocity in the original Eaton method, so as to improve

the prediction accuracy of pore pressure. The current development of VSP (vertical seismic profile) technology provides strong support for the application of this method. Honghai [17] further proposed an empirical model of acoustic velocity, taking into account the effects of porosity, mud content, and vertical effective stress, arguing that this model was suitable for sand and mudstone without the restriction of the undercompaction mechanism.

At present, a series of research achievements have been made in monitoring primary abnormally high pressure caused by undercompaction and fluid expansion. However, in recent years, pressure relief formation has been drilled frequently and the difficulty and error of pressure monitoring are extremely great, which leads to frequent field leakage and stuck drilling accidents that seriously affect casing depth and engineering safety. At present, the evaluation method of relief pressure formation is still based on the primary pressure evaluation method, that is, the Eaton and Bowers methods are used for evaluation on the basis of seismic and logging data. The adaptability of this method to abnormal pressure of the relief pressure formation is poor, so it is urgent to establish an effective evaluation method for the pressure of relief formation. Therefore, a pore pressure transfer model under the coupling effect of seepage and stress was established in this paper on the basis of well data and the distribution range of the pressure relief zone in the study area and its internal pressure distribution were determined, which can improve the foundation for pressure predictions for new drilling in this area.

2. Physical Model

Overpressure release is an effect of lowering abnormally high pressure to hydrostatic pressure. Overpressure release can be classified as complete and incomplete release. If a certain overpressure state is maintained after overpressure release, this is called incomplete release; otherwise, it is called complete release. Relief-type overpressure is the residual low amplitude overpressure after incomplete release.

There are many ways to release abnormally high pressure; the common ones are faults, cracks, sand bodies, etc. The result of pressure release leads to pressure redistribution in a certain range around the pressure release channel. In order to quantitatively describe the pressure relief range and the redistribution of pressure, the physical model of the pressure relief zone is simplified as shown in Figure 1:

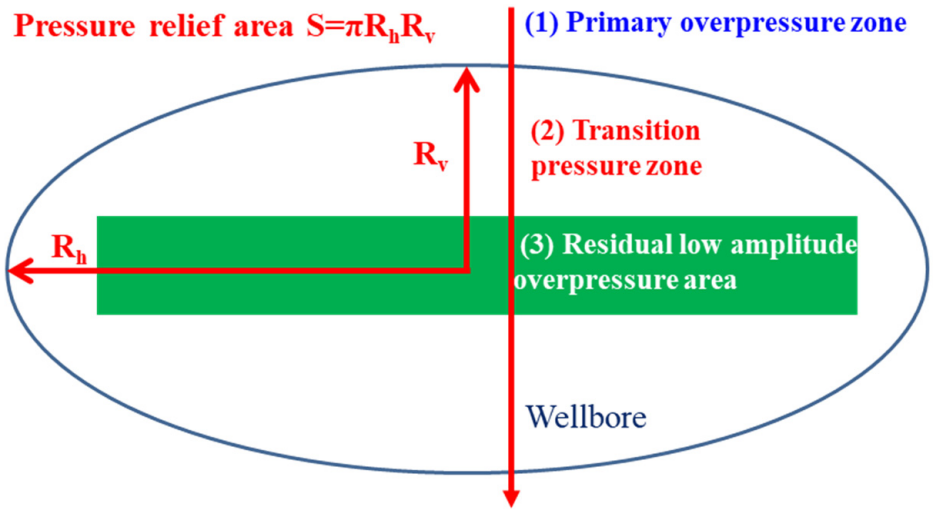

Figure 1. The physical model of the pressure relief zone.

The pressure zone after pressure relief can be divided into three parts: (1) primary overpressure zone; (2) transition pressure zone; and (3) residual low amplitude overpressure area. The range of pressure relief can be quantitatively characterized by the following parameters: (1) lateral pressure relief radius R_h: the horizontal distance from the center point of the low amplitude overpressure layer to the boundary of the pressure relief range;

(2) longitudinal pressure relief radius Rv: the vertical distance from the center point of the low amplitude overpressure layer to the boundary of the pressure relief range; and (3) pressure relief area S: In relatively homogeneous strata, the pressure relief area on the vertical profile is elliptical in shape, and its area is the pressure relief area.

3. Governing Equations

3.1. Deformation

(1) Effective stress principle

According to the effective stress principle, the deformation of the skeleton is only related to the effective stress. For saturated porous media, the effective stress is defined as:

$$\sigma'_{ij} = \sigma_{ij} - \alpha_{\mathrm{b}} p \delta_{ij} \tag{1}$$

The effective stress coefficient can be expressed as:

$$\alpha_{\mathrm{b}} = 1 - \frac{K_{\mathrm{fr}}}{K_{\mathrm{m}}} \tag{2}$$

(2) Equilibrium equation

The equilibrium equation of the skeleton is written as:

$$\sigma'_{ij,j} + F_{\mathrm{b}i} = 0 \tag{3}$$

(3) Geometric equation

The geometric equation is:

$$\varepsilon_{ij} = \frac{1}{2}\left(u_{i,j} + u_{j,i}\right) \tag{4}$$

The strain coordination equation can be derived from Equation (4):

$$\left.\begin{array}{c} \frac{\partial^2 \varepsilon_x}{\partial y^2} + \frac{\partial^2 \varepsilon_y}{\partial x^2} = \frac{\partial^2 \gamma_{xy}}{\partial x \partial y} \\ \frac{\partial^2 \varepsilon_y}{\partial z^2} + \frac{\partial^2 \varepsilon_z}{\partial y^2} = \frac{\partial^2 \gamma_{yz}}{\partial y \partial z} \\ \frac{\partial^2 \varepsilon_z}{\partial x^2} + \frac{\partial^2 \varepsilon_x}{\partial z^2} = \frac{\partial^2 \gamma_{zx}}{\partial z \partial x} \\ 2\frac{\partial^2 \varepsilon_x}{\partial y \partial z} = \frac{\partial}{\partial x}\left(-\frac{\partial \gamma_{yz}}{\partial x} + \frac{\partial \gamma_{xz}}{\partial y} + \frac{\partial \gamma_{xy}}{\partial z}\right) \\ 2\frac{\partial^2 \varepsilon_y}{\partial z \partial x} = \frac{\partial}{\partial y}\left(\frac{\partial \gamma_{yz}}{\partial x} - \frac{\partial \gamma_{xz}}{\partial y} + \frac{\partial \gamma_{xy}}{\partial z}\right) \\ 2\frac{\partial^2 \varepsilon_z}{\partial x \partial y} = \frac{\partial}{\partial z}\left(\frac{\partial \gamma_{yz}}{\partial x} - \frac{\partial \gamma_{xz}}{\partial y} - \frac{\partial \gamma_{xy}}{\partial z}\right) \end{array}\right\} \tag{5}$$

(4) Constitutive equation

The constitutive relation adopts the generalized Hooke's law:

$$\varepsilon_{ij} = \frac{1}{2G_{\mathrm{fr}}}\sigma'_{ij} - \frac{\lambda_{\mathrm{fr}}}{2G_{\mathrm{fr}}(3\lambda_{\mathrm{fr}} + 2G_{\mathrm{fr}})}\delta_{ij}\sigma'_{kk} \tag{6}$$

Or written as:

$$\sigma'_{ij} = \lambda_{\mathrm{fr}}\delta_{ij}\varepsilon_{kk} + 2G_{\mathrm{fr}}\varepsilon_{ij} \tag{7}$$

If the commonly used elastic modulus E_{fr} and Poisson's ratio v_{fr} are used to express Equation (7), then:

$$\sigma'_{ij} = \frac{E_{\mathrm{fr}} v_{\mathrm{fr}}}{(1 + v_{\mathrm{fr}})(1 - 2v_{\mathrm{fr}})}\varepsilon_{kk}\delta_{ij} + \frac{E_{\mathrm{fr}}}{1 + v_{\mathrm{fr}}}\varepsilon_{ij} \tag{8}$$

In this paper, the elastic modulus of the skeleton E_{fr} and bulk modulus K_{fr} of the skeleton were used to define the elastic properties of the formation. Equation (7) is written as follows:

$$\sigma'_{ij} = \left(K_{\mathrm{fr}} - \frac{2K_{\mathrm{fr}}E_{\mathrm{fr}}}{9K_{\mathrm{fr}} - E_{\mathrm{fr}}}\right)\delta_{ij}\varepsilon_{kk} + \frac{6K_{\mathrm{fr}}E_{\mathrm{fr}}}{9K_{\mathrm{fr}} - E_{\mathrm{fr}}}\varepsilon_{ij} \tag{9}$$

In combination with Equations (3) and (9), the equation can be written as:

$$\frac{6K_{\mathrm{fr}}E_{\mathrm{fr}}}{9K_{\mathrm{fr}} - E_{\mathrm{fr}}}u_{,ii} + \left(K_{\mathrm{fr}} - \frac{2K_{\mathrm{fr}}E_{\mathrm{fr}}}{9K_{\mathrm{fr}} - E_{\mathrm{fr}}}\right)e_{,i} + F_{\mathrm{b}i} = 0 \tag{10}$$

Equation (10) is the skeleton coupling elastic deformation equation. The coupling term of the fluid seepage effect is reflected in the first two terms of the equation. The stress used in the first two terms of the equation must be the effective stress, while the influence of body force, such as gravity, is reflected in the last term.

The above skeleton coupling deformation equations can only be solved by simultaneous seepage field equations.

3.2. Fluid Flow

According to the generalized Darcy's law, the relative velocity of the liquid v_i^{lr} is written as:

$$v_i^{\mathrm{lr}} = \phi\left(v_i^{\mathrm{l}} - v_i^{\mathrm{s}}\right) = -\frac{k_{ij}^{\mathrm{l}}}{\mu^{\mathrm{l}}}\left(p_{,j}^{\mathrm{l}} + \rho_{\mathrm{l}}g_j\right) \tag{11}$$

Note that in order to distinguish the tensor index symbols i, j and the named symbols l, s, lr, and lT when a tensor requires both of these symbols, the tensor index symbols are uniformly written in the subscript and the named symbols are uniformly written in the superscript.

Since the mass of fluid flowing into the unit in unit time is equal to the increase in the liquid storage in the unit, the mass conservation equation of fluid is:

$$\frac{\partial}{\partial t}\left(\phi\rho^{\mathrm{l}}\right) = -\partial_{,i}\left(\phi\rho^{\mathrm{l}}v_i^{\mathrm{l}}\right) \tag{12}$$

Equation (12) can be further written as:

$$\partial_{,i}\left[\frac{\rho^{\mathrm{l}}k_{ij}^{\mathrm{l}}}{\mu^{\mathrm{l}}}\left(p_{,j}^{\mathrm{l}} + \rho^{\mathrm{l}}g_j\right)\right] = \phi\frac{\partial\rho^{\mathrm{l}}}{\partial t} + \rho^{\mathrm{l}}\frac{\mathrm{d}\phi}{\mathrm{d}t} \tag{13}$$

If the pore pressure affects the fluid density, the derivative of fluid density concerning time can be written as:

$$\frac{\mathrm{d}\rho^{\mathrm{l}}}{\mathrm{d}t} = \frac{\partial\rho^{\mathrm{l}}}{\partial p^{\mathrm{l}}}\frac{\partial p^{\mathrm{l}}}{\partial t} = \rho^{\mathrm{l}}\alpha_{\mathrm{p}}\frac{\partial p^{\mathrm{l}}}{\partial t} \tag{14}$$

where α_{p} is the compressibility coefficient of the fluid, defined as:

$$\alpha_{\mathrm{p}} = \frac{1}{\rho^{\mathrm{l}}}\frac{\partial\rho^{\mathrm{l}}}{\partial p^{\mathrm{l}}} \tag{15}$$

Considering the dynamic change of porosity, there is:

$$\frac{\partial}{\partial t}[(1-\phi)\rho^{\mathrm{s}}] = -\partial_{,i}[(1-\phi)\rho^{\mathrm{s}}v_i^{\mathrm{s}}] \tag{16}$$

Or written as:

$$\frac{\mathrm{d}\phi}{\mathrm{d}t} = \frac{1-\phi}{\rho^{\mathrm{s}}}\frac{\mathrm{d}\rho^{\mathrm{s}}}{\mathrm{d}t} + (1-\phi)\frac{\partial e}{\partial t} \tag{17}$$

If the influence of pore pressure and skeleton deformation on seepage is considered, at the same time, the coupling single-phase seepage equation can be obtained simultaneously by Equations (13), (14), and (17):

$$\partial_{,i}\left[\frac{\rho^{\mathrm{l}}k_{ij}^{\mathrm{l}}}{\mu^{\mathrm{l}}}\left(p_{,j}^{\mathrm{l}}+\rho^{\mathrm{l}}g_{j}\right)\right]=\phi\alpha_{\mathrm{p}}\frac{\partial p^{\mathrm{l}}}{\partial t}+\frac{1-\phi}{\rho^{\mathrm{s}}}\frac{\mathrm{d}\rho^{\mathrm{s}}}{\mathrm{d}t}+(1-\phi)\frac{\partial e}{\partial t} \tag{18}$$

In Equation (18), the second and third items on the right reflect the influence of skeleton deformation on seepage, the second item on the left reflects the influence of gravity, and the first item on the right reflects fluid compressibility. Equation (18) requires simultaneous skeleton deformation field equations to be solved.

In particular, when the flow velocity is large, the movement of the fluid gradually deviates from Darcy's law. At this time, the nonlinear seepage law should be adopted. Forchheimer's law is used to describe the general seepage process in the form of:

$$\boldsymbol{f}(1+\beta\sqrt{\boldsymbol{v}_{\mathrm{l}}\cdot\boldsymbol{v}_{\mathrm{l}}})=-\frac{k_{\mathrm{s}}}{\gamma_{\mathrm{l}}}\boldsymbol{k}\cdot\left(\frac{\partial p^{\mathrm{l}}}{\partial \boldsymbol{x}}-\rho^{\mathrm{l}}\boldsymbol{g}\right) \tag{19}$$

The bold type in the formula represents the invariant notation of the vectors.

The permeability coefficient $\overline{\boldsymbol{k}}$ is defined as:

$$\overline{\boldsymbol{k}}=\frac{k_{\mathrm{s}}}{\left(1+\beta\sqrt{\boldsymbol{v}_{\mathrm{l}}\cdot\boldsymbol{v}_{\mathrm{l}}}\right)}\boldsymbol{k} \tag{20}$$

Therefore, Forchheimer's law can also be written as:

$$\boldsymbol{f}=-\frac{\overline{\boldsymbol{k}}}{\gamma_{\mathrm{l}}}\cdot\left(\frac{\partial p_{\mathrm{l}}}{\partial \boldsymbol{x}}-\rho_{\mathrm{l}}\boldsymbol{g}\right) \tag{21}$$

Permeability $\boldsymbol{k}$ of completely saturated porous media can be obtained through permeability experiments at low flow rates, which can be defined as a function of porosity.

Porosity can be derived from porosity, i.e., $e=\phi/(1-\phi)$. When the anisotropy of permeability is not considered, it is considered that the permeability is $\boldsymbol{k}$ in all directions. Due to formation sedimentation, it is sometimes necessary to consider the difference between horizontal and vertical permeability, which is recorded as k_{v} and k_{h}, respectively.

4. Numerical Methodology

4.1. Model Establishment

In this paper, the geomechanical model of the whole study area was established based on the geological survey results of the area. Then, the magnitude and direction of tectonic stress and formation pressure values at certain test wells were calculated by trial calculations of different boundary displacements and relief layer pressures until they were in general agreement with the actual measured values. Finally, the stress and formation pressure fields corresponding to the model with the best fit of the calculated values to the measured values were taken as the final results.

The overall equilibrium equation of the model structure was:

$$\boldsymbol{K}\delta=\boldsymbol{F}_{\mathrm{g}}+\boldsymbol{F}_{\mathrm{u}} \tag{22}$$

The stress was calculated as:

$$\boldsymbol{\sigma}=\boldsymbol{DB}\delta \tag{23}$$

Let there be N points within the model domain with measured stress values σ_1 (j), σ_2 (j), and σ_3 (j) assigned with the corresponding weight coefficients ω_1 (j), ω_2 (j), and ω_3 (j), respectively, according to the number of measurements and the confidence level. Using a certain constructive stress parameter T (determined by $\boldsymbol{F}$) positive problem solution, the

stress values were obtained as $\sigma'_1(j)$, $\sigma'_2(j)$, and $\sigma'_3(j)$, considering T as a change point in m-dimensional space, i.e., $T = T(T_1,T_2,T_3, \ldots ,T_m)$. Then, the sum of squares of the difference between $\sigma(j)$ and $\sigma_1(j)$ (the fitting criterion) was:

$$E(k) = \sum_{j=1}^{N} \omega_1(j)\left[\sigma_1(j) - \sigma'_1(j)\right]^2 + \sum_{j=1}^{N} \omega_2(j)\left[\sigma_2(j) - \sigma'_2(j)\right]^2 + \sum_{j=1}^{N} \omega_3(j)\left[\sigma_3(j) - \sigma'_3(j)\right]^2 \quad (24)$$

The magnitude of $E(k)$ can then be used as a measure of whether T is realistic, such that the inverse problem was transformed into an optimization problem, i.e., finding T (or $\boldsymbol{F}$) such that the optimality conditions were satisfied as:

$$\hat{E}(k) = \min E(k) \quad (25)$$

The constraints were taken as:

$$0 \le T_i \le \max\sigma_1(j) \quad (26)$$

The stresses and stress directions could be obtained by solving the above mechanical equations (by finite element means). In the actual study, the internal and external load method was mainly used, and the simulated values were optimally fitted to the measured values by adjusting the internal and external load values based on the established intrinsic structure model. Of course, the reasonableness of the results of ground stress inversion by the above method was mainly influenced by the following factors: (1) the shape and size of the geometric model; (2) the selection of the regional structural lattice; (3) the determination of the boundary conditions; (4) the selection of the mechanical model; and (5) the criterion of the best fit between the calculated and measured values.

4.2. Study Area

This paper, taking well block X as an example, aimed to calculate the pore pressure distribution on the profile of section A, determining the vertical and horizontal pore pressure relief range, namely the horizontal and vertical pore pressure relief radii, and the drainage area. Well block X was located at the northeast wing of the M structure in the central diapir zone of Ledong District, Yinggehai Basin (Figure 2). Table 1 shows the basic technical data of the individual geological layers. The trap types of the Yinggehai and Huangliu Formations are mainly structural and lithologic traps.

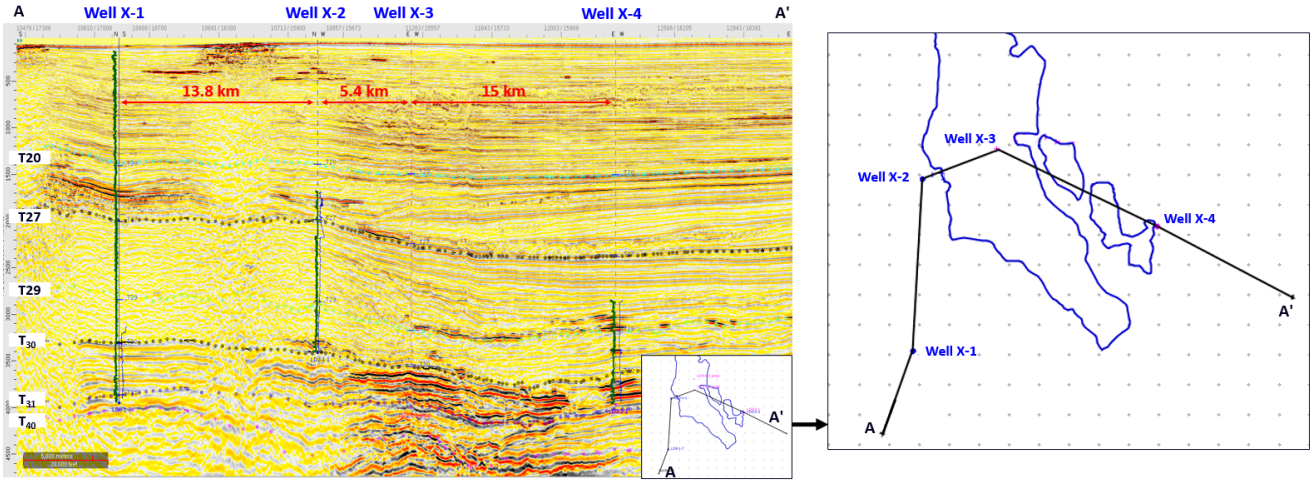

Figure 2. Well trajectory on section A of well block X.

Table 1. Basic technical data of the individual geological layers.

Stratigraphic System				Seismic Interface	Top Interface	Time (ms)	Altitude (-m)	Thickness (m)	Temperature (°C)
System	Series	Formation	Member						
Quaternary	Holocene pleistocene	Ledong		Seabed			95		
Neogene	Pliocene	Yinggehai	No. 1	T20		1422	1490		77
			No. 2	T27		1945	2245		109
				T29		2553	3170		148
					N_2ygh^2 A	2763	3481	20	161
					N_2ygh^2 B	2802	3530	30	163
	Miocene	Huangliu	No. 1	T30		2819	3560		164
					N_1hl^1 B	2866	3633	60	167
					N_1hl^1 C	2918	3726	29	171
					N_1hl^1 D	2945	3778	74	173
					N_1hl^1 E	3002	3891	36	178
			No. 2	T31		3020	3928		179
				TD		3032	3952		181

4.3. Model Parameters

The geometric model of profile A was established, setting the initial porosity, initial permeability, Young's modulus, and Poisson's ratio to vary with space on the profile. The pressure profiles of wells X-1, X-2, and X-4 were taken as the constraint condition, using the method of steady-state seepage on profile A to establish the pressure balance of profile A and taking well X-3 as the verification well to verify the reliability of the model.

The software program Abaqus was used for the simulations with 270,000 finite elements and 271,331 nodes. The type of finite elements was CPE4P (a 4-node plane strain quadrilateral with bilinear displacement and bilinear pore pressure).

The boundaries of the left and right were only free in the vertical direction. The bottom of the geometric model possessed constraints in both vertical and horizontal directions. The pressure profiles of wells X-1, X-2 and X-4 were also used as constraints. The initial values of elastic modulus, Poisson's ratio, density, porosity, permeability, and pore pressure are shown in Figures 3–6.

The porosity, permeability, and density parameters near each well were given, and the parameters of the cross-well area were approximately replaced by the linear interpolation method. Taking well X-3 as an example, its initial porosity, permeability, and density are shown in Figure 3.

The change in formation pressure will lead to formation rock deformation and then affect the change in formation porosity and permeability. As shown in Figure 4, this paper considered the dynamic change in permeability with porosity. The solid line was an approximation of the actual survey.

As shown in Figure 5, the elastic model of well block X and Poisson's ratio change with depth are given.

According to the early drilling and completion data and correction, the pressure profiles of wells X-1, X-2 and X-4 are shown in Figure 6, and the pressures of these three wells were used as constraints. The traditional Eaton's method, based on the acoustic velocity data, was used to formulate the preliminary pressure profiles of wells X-1, X-2, and X-4, and the pressure test data using MDT (modular formation dynamics tester) were employed to determine the ultimate pressure profiles.

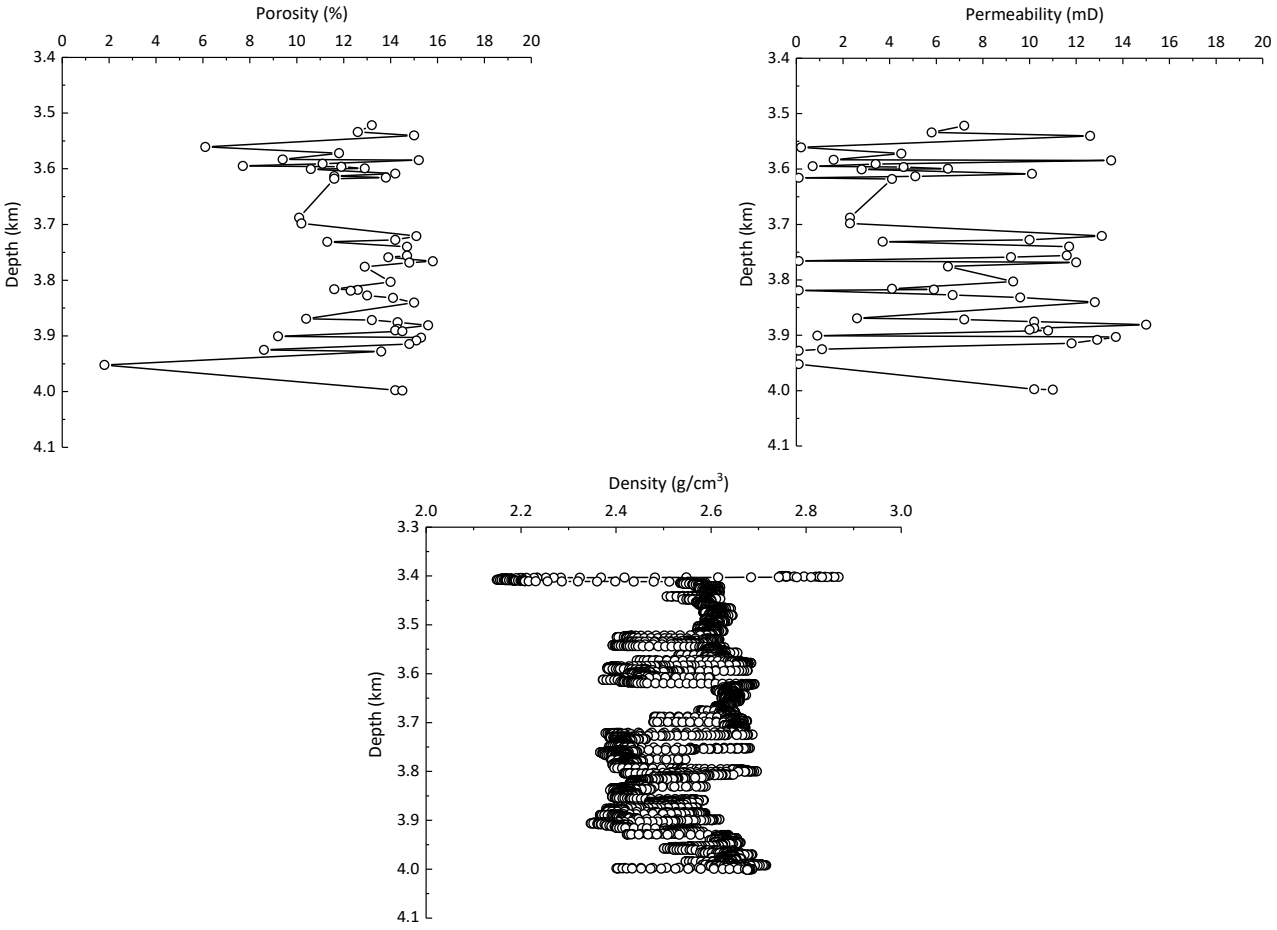

Figure 3. Changes in initial porosity, permeability, and density with depth near well X-3.

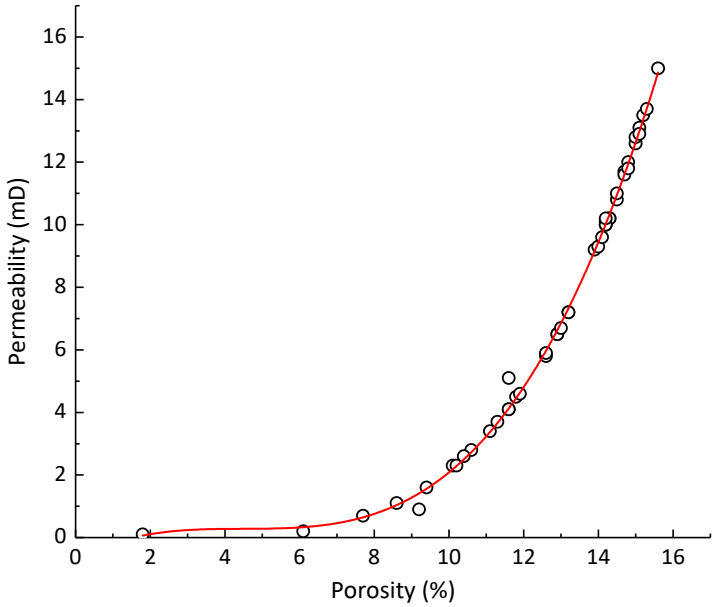

Figure 4. Permeability changes with porosity near well X-3.

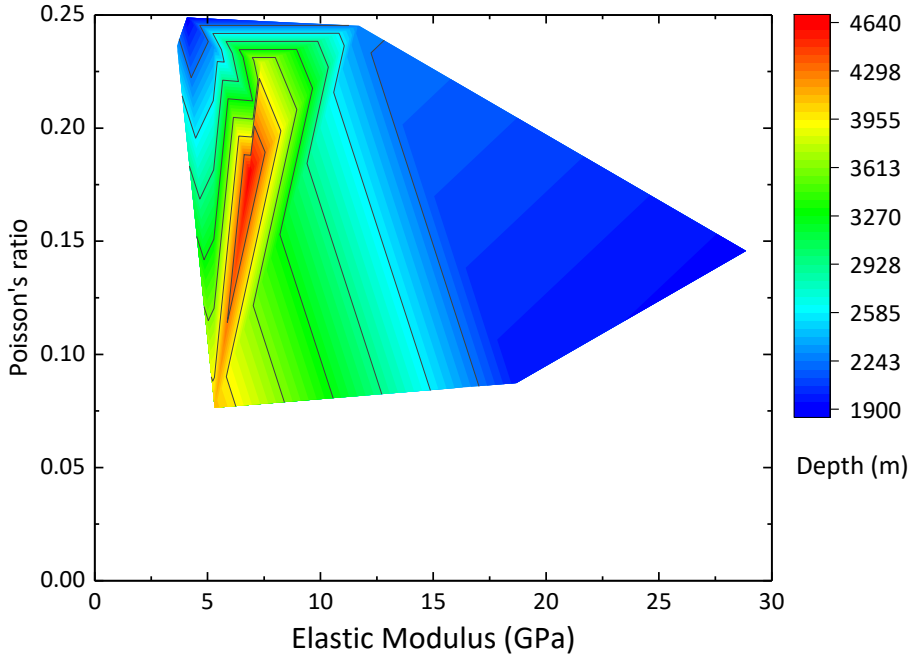

Figure 5. Elastic model and Poisson's ratio variation with depth in well block X.

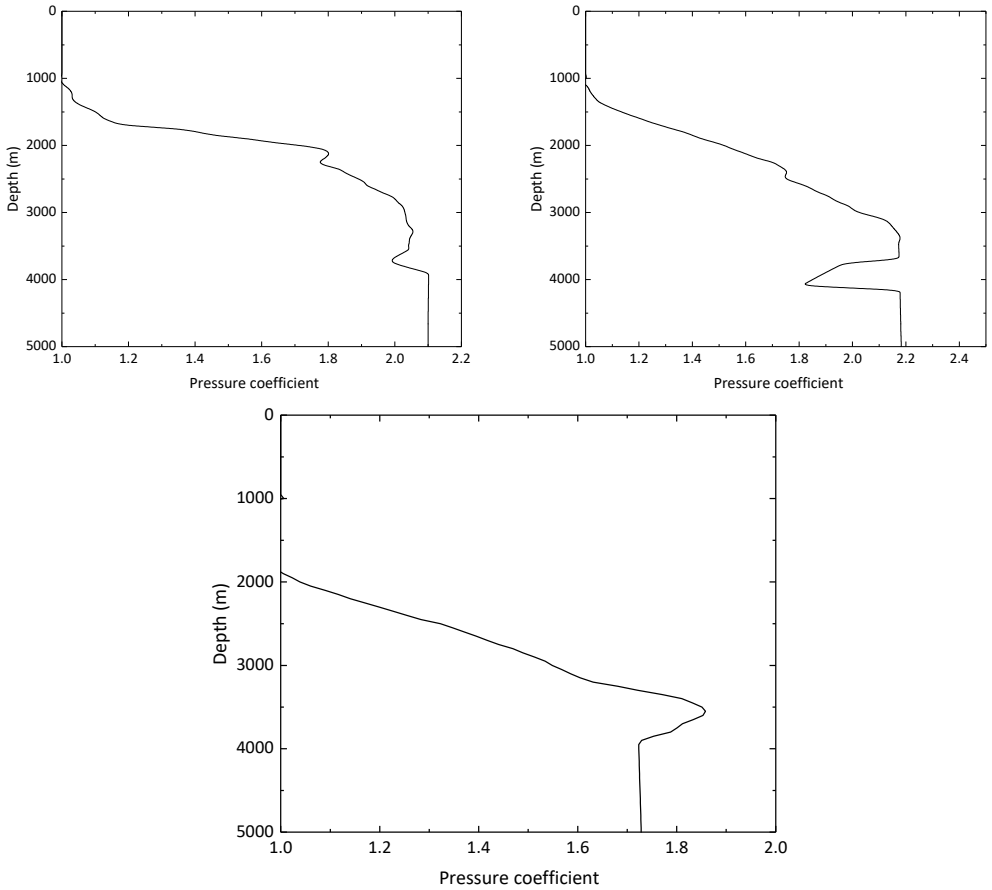

Figure 6. Pressure profile of wells X-1, X-2, and X-4.

5. Results

5.1. Model Validation

As shown in Figure 7, the reliability of the model was verified by the pore pressure calculation results of well X-3. It can be seen from the figure that the measured pressure

value of the pressure relief layer and its lower part fell near the predicted value, indicating that the model was reliable. As shown in Figure 7, 14 MDT pore pressure test data were compared with the predicted pore pressure by the numerical models. The calculation error was approximately 3.32% at the depth of 3879 m. The pore pressure caused by the pressure relief of the sand body (coefficient = 1.46) kept a similar value and trend with the data in the literature (coefficient = 1.55) [18]. At present, the measured pore pressure data were relatively sparse and concentrated at two depths (3600 and 3800 m). More data at other depths (this well or near well) will be used for verification if field test data are collected.

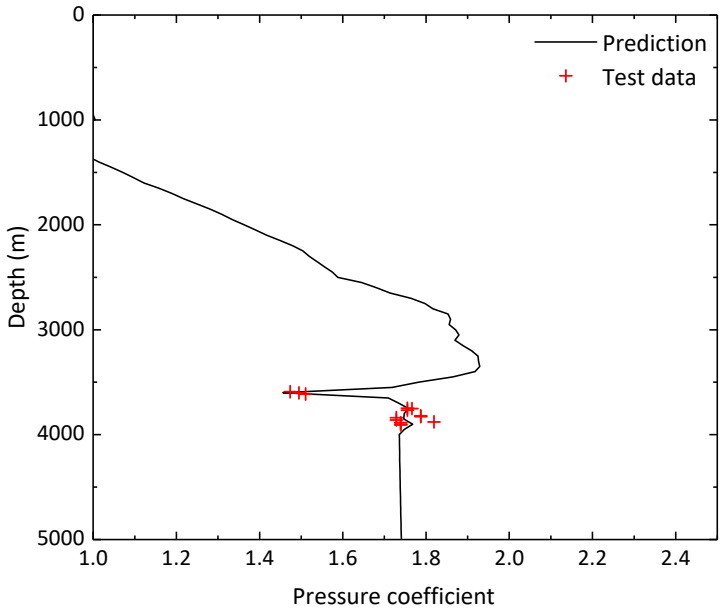

Figure 7. Comparison and verification of measured and predicted pressure of well X-3.

5.2. Results of Pore Pressure Relief

Figure 8 shows the value of the pressure coefficient at any position on section A, as predicted by the coupled hydro-mechanical model. In this regard, obtaining the pore pressure test data of drilled wells and determining the hydro-mechanical coupled parameters are important. Only in this way can the numerical model obtain reliable results. The traditional Eaton's method, based on the acoustic velocity data, was used to formulate the preliminary pressure profiles of wells X-1, X-2, and X-4, and the pressure test data using MDT (modular formation dynamics tester) were employed to determine the ultimate pressure profiles. The pressure profiles of wells X-1, X-2, and X-4 were used as constraints. The pore pressure coefficients near all wells in Figure 8 showed the same values and trends compared with Figures 6 and 7.

Figure 9 shows the pressure relief area around wells X-3 and X-2. Figure 9 shows an enlarged exhibit near wells X-3 and X-2 of Figure 8. The pore pressure coefficients near all wells in Figure 9 showed the same values and trends compared with Figures 6 and 7.

In combination with the above physical model, this paper quantitatively estimated the lateral pressure relief radius, longitudinal pressure relief radius, and pressure relief area around different wells (as shown in Figure 10). It can be seen from the figure that the lateral pressure relief radius on profile A was 3000~6000 m, the lateral pressure relief range near well X-4 was the largest, and the lateral pressure relief range near well X-3 was the smallest. The longitudinal pressure relief range was obviously smaller than the transverse pressure relief range, between 100~500 m, and the longitudinal pressure relief range near well X-3 was the largest. The pressure relief area was 100×10^4~800×10^4 m^2, and the pressure relief area of well X-4 was the largest. The pressure relief range is related to the porosity and permeability characteristics around the well.

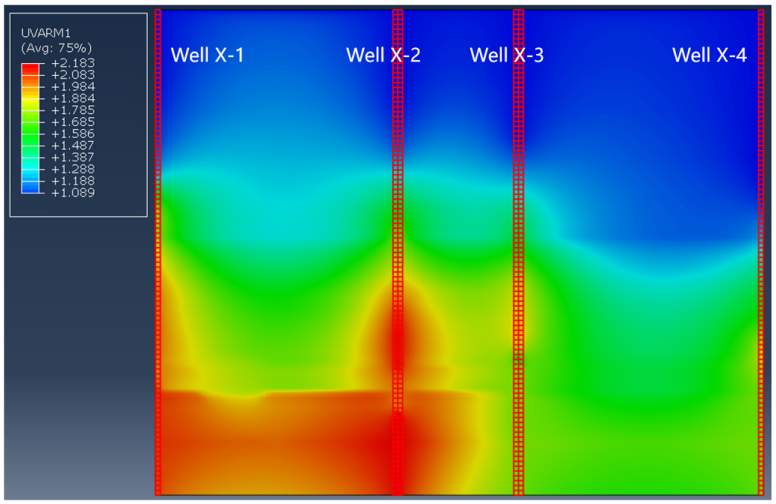

Figure 8. Values of the pressure coefficient at any position in profile A.

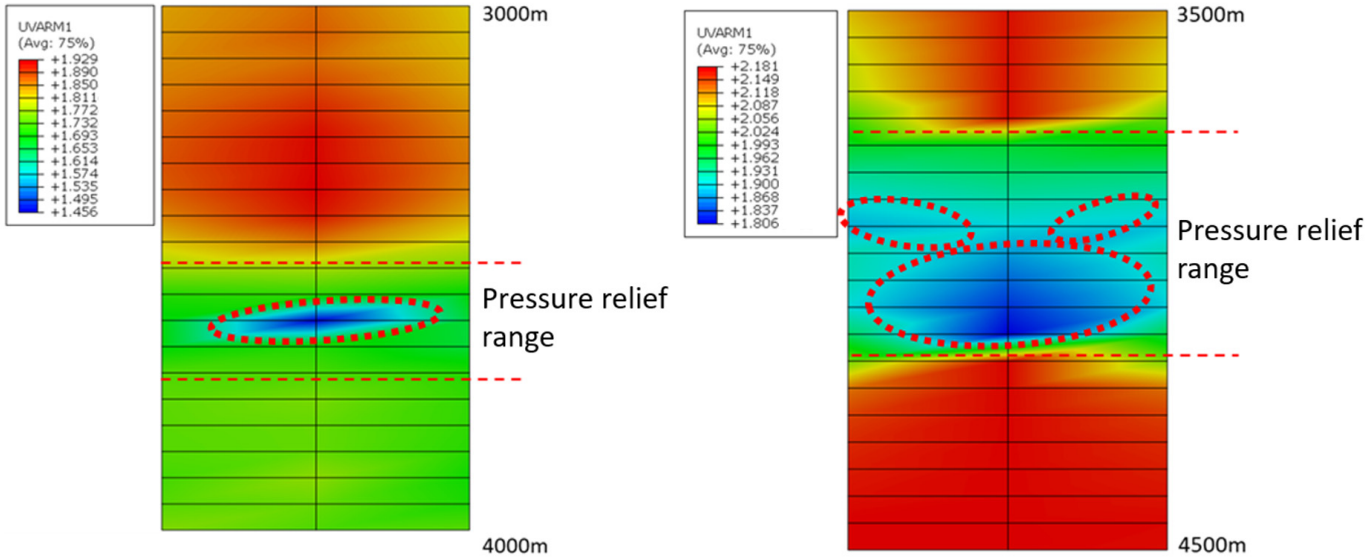

Figure 9. Pressure relief area around wells X-3 and X-2.

The horizontal pressure relief radius depends on the sand body's horizontal distribution, permeability, and pore pressure relief degree. A wider horizontal distribution, higher permeability, or greater degree of pore pressure relief leads to a larger horizontal pressure relief radius [19,20]. For the vertical pressure relief radius, the predicted data were approximate to the data shown in Figures 6 and 7. For the pressure relief area, these data could be calculated by the physical model of the pressure relief zone, as shown in Figure 1.

According to the model proposed in this paper, the undrilled pore pressure on section A could be predicted. Figure 11 shows the pore pressure prediction profile of an undrilled well, 3262 m to the left of well X-2. The pore pressure changes with depth showed the same trends compared with the two adjacent wells. It can be seen from the figure that there was no obvious pressure relief in this well and there was a small pressure relief between 3500 and 4000 m, so the density of drilling fluid within this depth range could be appropriately adjusted.

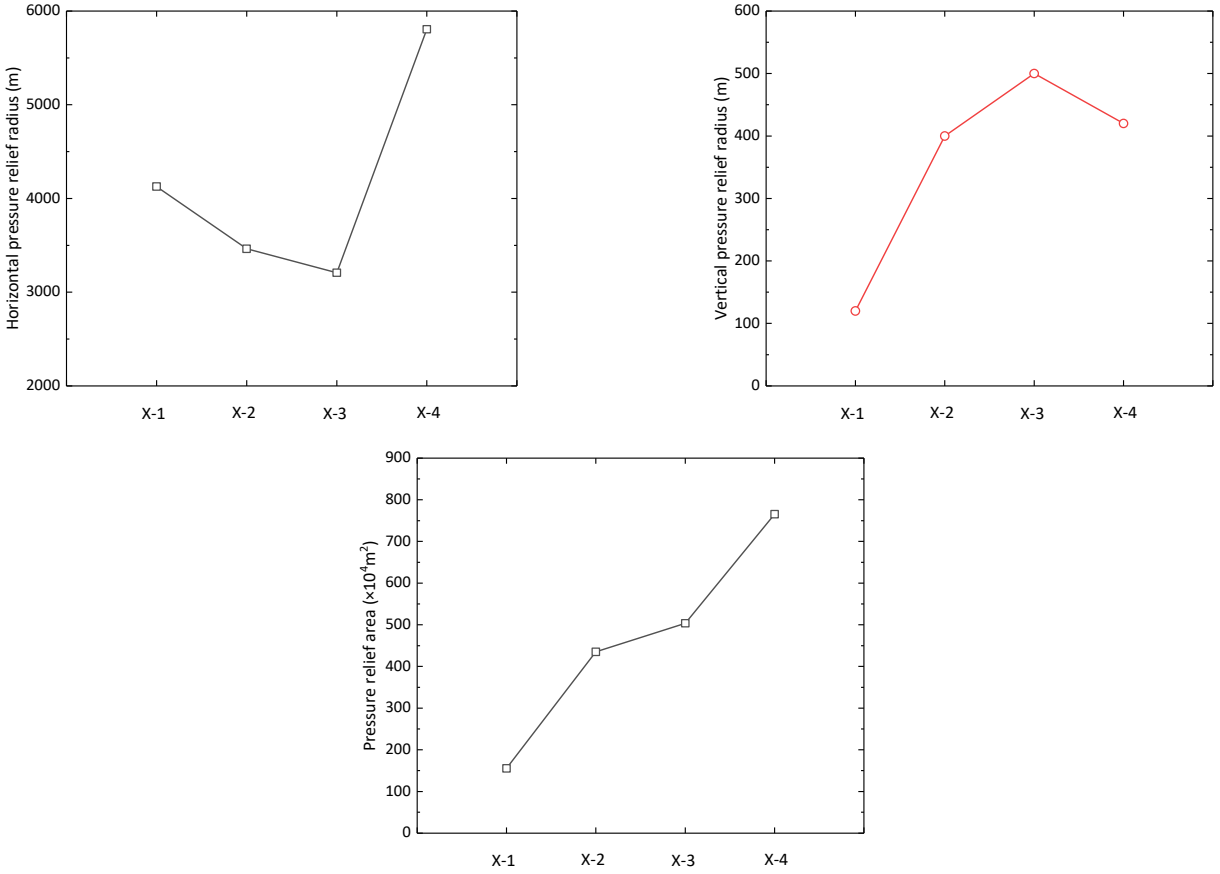

Figure 10. Transverse relief radius, longitudinal relief radius, and relief area around each well on profile A.

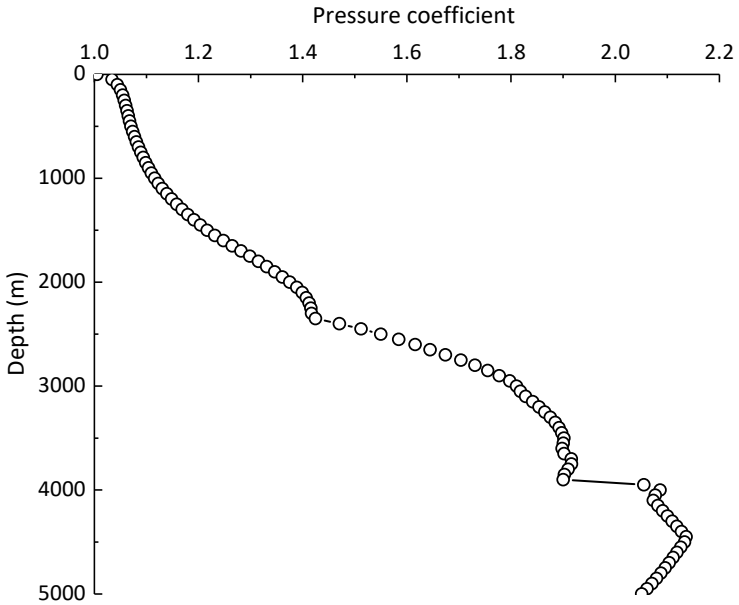

Figure 11. Prediction of the undrilled pore pressure profile.

5.3. Factors Affecting Pressure Distribution

5.3.1. Porosity and Permeability

The higher the porosity and permeability, the greater the degree of pressure relief. This means that the wider the horizontal distribution of the sand body, the larger the lateral pressure relief radius. The thicker the sand body, the larger the longitudinal relief radius.

Taking the well blocks X and N as examples for comparative analysis, it can be seen that the permeability of well block X was approximately 10 mD, while that of well block N was generally lower than 5 mD (Figure 12). The lateral pressure relief radius of well block X was approximately 3000~6000 m, while that of well block N was generally less than 800 m (Figure 13). Therefore, permeability determined the influence range of pressure relief.

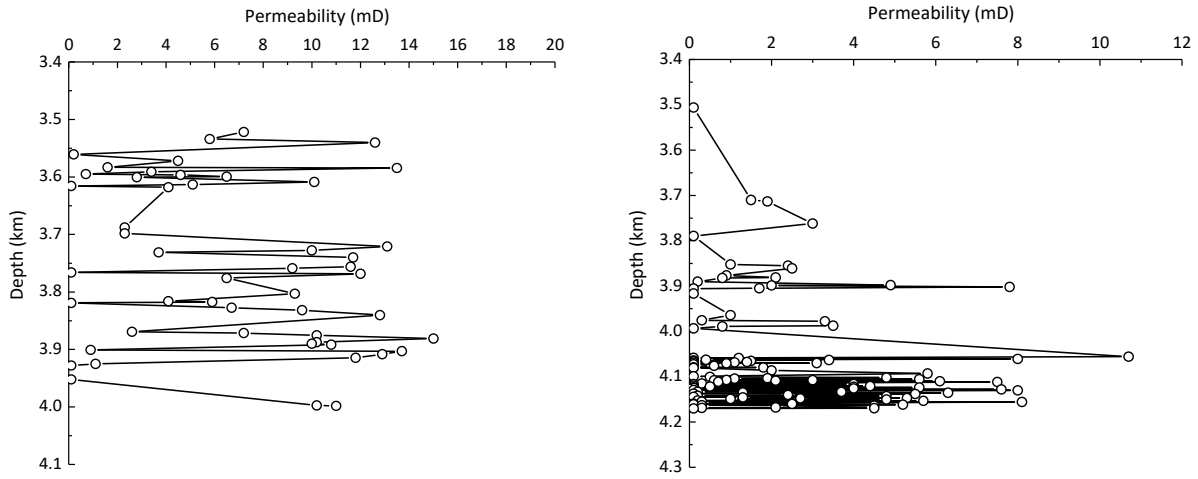

Figure 12. Permeability comparison between well blocks X and N.

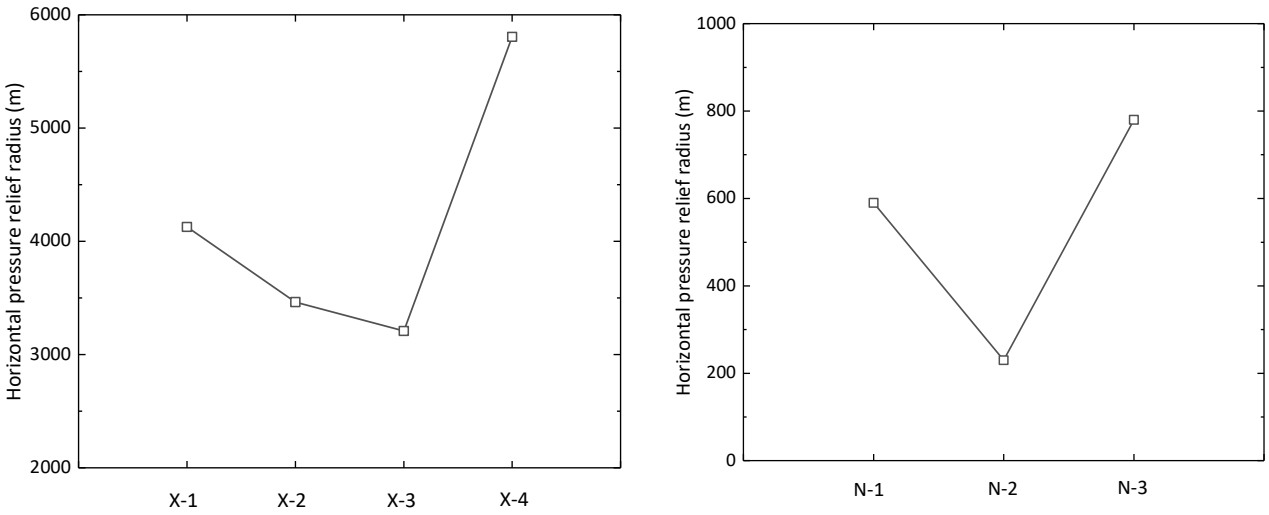

Figure 13. Comparison of lateral pressure relief radius between well blocks X and N.

5.3.2. Geotectonic Movement

The overpressure fluid in Yinggehai Basin was closed in the early stage and discharged intensively through the diapir in the late stage [21]. This paper analyzed the influence of diapir-induced fracture or hypertonic fracture opening on pressure relief. Taking the structure of well X-3 as an example, and referring to the pressure relief section monitored on-site, strata within the same depth range were intercepted for two-dimensional geological modeling, focusing on the pressure relief effect of lateral sand bodies and high permeability fractures and analyzing pressure changes in the formation before and after the opening of the diapir induced high permeability fractures (Figure 14).

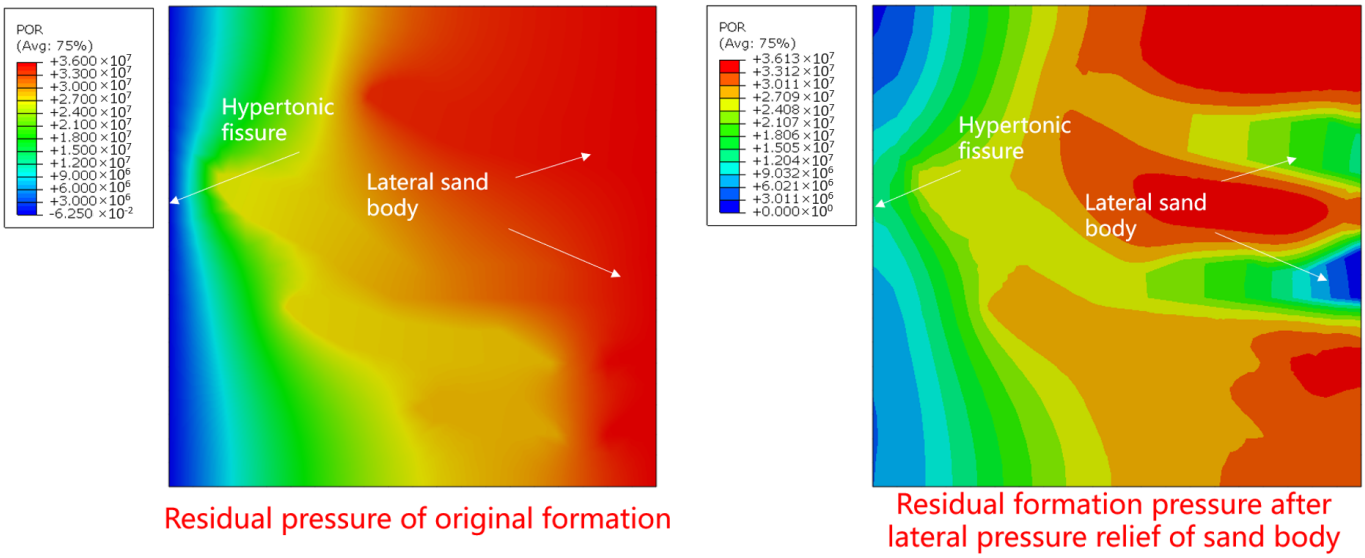

Figure 14. Formation pressure changes before and after the opening of diapir induced high permeability fractures.

The process of lateral pressure relief of the sandstone reservoir was simulated by using finite element simulation software. Figures 12 and 14 show the influence of porosity, permeability, and geological movement on pressure relief. A wider horizontal distribution, higher permeability, or greater degree of pore pressure relief led to a larger horizontal pressure relief radius. The results showed that the original high-pressure source in the sandstone reservoir released pressure due to the existence of transversely distributed high-permeability sand bodies and fractures at the boundary.

6. Summary and Conclusions

This paper proposed a pressure relief-type overpressure distribution prediction model based on seepage and stress coupling. A case study was conducted to numerically predict the pore pressure considering pore pressure relief using the finite element method. Several conclusions can be drawn, as follows:

(1) A physical model of the pressure relief zone was established. The pressure zone after pressure relief can be divided into three parts: primary overpressure zone, transition pressure zone, and residual low amplitude overpressure area. The range of pressure relief can be quantitatively characterized by the following parameters: lateral pressure relief radius, longitudinal pressure relief radius, and pressure relief area.

(2) In the case study, the measured pressure value of the pressure relief layer and its lower part fell near the predicted value, indicating that the model was reliable. This paper quantitatively estimated the lateral pressure relief radius, longitudinal pressure relief radius, and pressure relief area around different wells, finding that the pressure relief range was related to the porosity and permeability characteristics around the well.

(3) The influence of the laws of porosity, permeability, and geological movement on pressure relief were analyzed, revealing that higher porosity and permeability led to a greater degree of pressure relief. The wider the sand body is horizontally distributed, the larger the lateral pressure relief radius. The thicker the sand body, the larger the longitudinal relief radius. The opening of the diapir induced hyperpermeability fractures that will result in formation pressure relief. The research results provide a new method for the prediction of pressure relief-type overpressure that will improve the basic guarantee of safe and efficient drilling of this kind of formation.

Author Contributions: Methodology, Y.G.; validation, C.W.; investigation, G.L.; data curation, Y.S.; writing—original draft preparation, G.L.; supervision, S.G.; funding acquisition, Y.G. All authors have read and agreed to the published version of the manuscript.

Funding: This work would not be possible without financial support from the National Natural Science Foundation of China (No. 52204048), the Young Talent Fund of University Association for Science and Technology in Shaanxi, China (No. 20210413), and the Scientific Research Program funded by Shaanxi Provincial Education Department (No. 21JK0937).

Data Availability Statement: Not applicable.

Acknowledgments: We are grateful to CNOOC China Ltd. (Hainan) for providing us with a compressive set of reservoir data.

Conflicts of Interest: The authors declare no conflict of interest.

Nomenclature

R_h: lateral pressure relief radius; R_v: longitudinal pressure relief radius; S: pressure relief area; σ'_{ij}: effective stress; σ_{ij}: total stress; α_b: effective stress coefficient; p: pore pressure; δ_{ij}: Kronecker tensor; K_{fr} and K_m: bulk moduli of rock skeleton and rock skeleton material, respectively; F_{bi}: skeleton force component in direction i (i = x,y,z); ε_{ij}: strain; u_i: displacement component in direction i; λ_{fr} and G_{fr}: lame constants of the skeleton, respectively; ε_{kk}: volume strain; E_{fr} and v_{fr}: elastic modulus and Poisson's ratio, respectively; e: volume strain of the skeleton; ϕ: porosity; v_i^l: absolute velocity of the liquid; $v_i^s = \partial u_i/\partial t$: deformation rate of the skeleton; k_{ij}^l: permeability coefficient of the liquid; p^l: liquid pressure; ρ^l: liquid density; g: gravitational acceleration; μ_1: viscosity of the fluid; α_p: compressibility coefficient of the fluid; ρ_s: skeleton density; $f = s\phi v_l$: volume flow rate of fluid per unit area of the porous medium or the effective velocity of fluid; s: fluid saturation, s = 1 is saturated medium, s = 0 is dry medium; v_l: velocity vector of the fluid; $\beta = \beta(e)$: velocity coefficient and function of porosity e; $k_s = k_s(s)$: influence of the degree of fluid saturation on permeability coefficient, when it is saturated porous medium (i.e., s = 1), k_s = 1; γ_l: specific gravity of the liquid; $\boldsymbol{k} = \boldsymbol{k}(e)$: permeability coefficient vector of saturated porous media, expressed as a function of porosity e; p_l: pressure of the fluid; $\boldsymbol{x}$: position vector; ρ^l: fluid density; **g:** gravitational acceleration vector; $\bar{k}$: permeability coefficient; K: unit stiffness matrix; δ: nodal displacement; F_g: overall load array of self-weight stresses; F_u: loaded array of structural stresses; $\boldsymbol{D}$: elasticity matrix; $\boldsymbol{B}$: geometric matrix and values of elements in the matrix depending on cell type and can be derived from the geometric equations of elastic mechanics.

References

1. Swarbrick, R.E.; Osborne, M.J. Mechanisms that generate abnormal pressure: An overview. In *Abnormal Pressure in Hydrocarbon Environments*; Law, B.E., Ulmishek, G.F., Slavin, V.I., Eds.; AAPG Memoir: Tulsa, OK, USA, 1998; Volume 70, pp. 13–43.
2. Bowers, G.L. Detecting high overpressure. *Lead. Edge* **2002**, *21*, 174–177. [CrossRef]
3. Ozkale, A. Overpressure Prediction by Mean Total Stress Estimate Using Well Logs for Compressional Environments with Strike-Slip or Reverse Faulting Stress State. Master's Thesis, Texas A&M University, College Station, TX, USA, 2006.
4. Fan, H.H. *Analysis Method and Application of Abnormal Formation Pressure*; Science Press: Beijing, China, 2016.
5. Tremosa, J.; Gaucher, E.C.; Gailhanou, H. Overpressure generation by smectite dehydration in sedimentary basins constrained by salinity dilution and stable isotopes. *Appl. Geochem.* **2021**, *131*, 105035. [CrossRef]
6. Bowers, G.L. Pore pressure estimation from velocity data: Accounting for overpressure mechanisms besides undercompaction. *SPE Drill. Complet.* **1995**, *10*, 89–95. [CrossRef]
7. Bowers, G.L. Determining an appropriate pore-pressure estimation strategy. In Proceedings of the Offshore Technology Conference, Houston, TX, USA, 30 April–3 May 2001.
8. Stephen, O.; Swarbrick, R.W.; Hoesni, J.; Lahann, R. Pore pressure prediction in challenging areas, Malay Basin, SE Asia. In Proceedings of the Thirty-Fifth Annual Convention & Exhibition, Jakarta, Indonesia, 18–20 May 2011.
9. Obradors-Prats, J.; Rouainia, M.; Aplin, A.C.; Crook, A.J.L. A diagenesis model for geomechanical simulations: Formulation and implications for pore pressure and development of geological structures. *J. Geophys. Res. Solid Earth* **2019**, *124*, 4452–4472. [CrossRef]
10. Fan, C.; Wang, G.; Wang, Z.; Han, X.; Chen, J.; Zhang, K.; Zhang, B. Prediction of multiple origin overpressure in deep fold-thrust belt: A case study of Kuqa subbasin, Tarim Basin, northwestern China. *AAPG Bull.* **2021**, *105*, 1511–1533. [CrossRef]
11. Gao, Y.; Chen, M.; Jiang, H. Influence of unconnected pores on effective stress in porous geomaterials: Theory and case study in unconventional oil and gas reservoirs. *J. Nat. Gas Sci. Eng.* **2021**, *88*, 103787. [CrossRef]
12. Song, X.; Yao, X.; Li, G.; Xiao, L.; Zhu, Z. A novel method to calculate formation pressure based on the LSTM-BP neural network. *Pet. Sci. Bull.* **2022**, *1*, 12–23.

13. Eaton, B.A. The equation for geopressure prediction from well logs. In Proceedings of the 50th Annual SPE Fall Meeting, Dallas, TX, USA, 28 September 1975.
14. Jincai, Z. Pore pressure prediction from well logs: Methods, modifications, and new approaches. *Earth-Sci. Rev.* **2011**, *108*, 50–63.
15. Khaksar, A. Depth limit of velocity-effective stress relationships for pore pressure prediction, implications for wellbore stability analysis. In Proceedings of the 45th US Rock Mechanics/Geomechanics Symposium, San Francisco, CA, USA, 26–29 June 2011.
16. Hua, Y.; Hilterman, F.J. Shear Wave Sensitivity to Pore Pressure Prediction. In Proceedings of the SEG Annual Meeting, Houston, TX, USA, 22–27 September 2013.
17. Fan, H. A new integrated pore pressure evaluation method for shale-sand formations. *Pet. Explor. Dev.* **2002**, *1*, 90–92.
18. Hu, Y.; Chen, P.; Liu, S. Difficulties and countermeasures of formation pressure monitoring while drilling in Yingqiong basin. *Mud Logging Eng.* **2020**, *31*, 41–49.
19. Xie, T. Natural gas migration conducting system and reservoir formation pattern in Southeast Hainan Basin. *Pet. Explor.* **2000**, *5*, 17–21.
20. Aiqun, L.; Caiwei, F.; Yong, D. Pressure structure and relationship with hydrocarbon accumulation in Nanhai Qiongdongnan high pressure basin. *Prog. Geophys.* **2017**, *32*, 1817–1822.
21. Fang, H.; Weiliang, D.; Huayao, Z.; Xusheng, Y. Overpressure fluid flow and rapid accumulation of natural gas in Yinggehai Basin. *Acta Pet. Sin.* **2003**, *24*, 7–12.

Disclaimer/Publisher's Note: The statements, opinions and data contained in all publications are solely those of the individual author(s) and contributor(s) and not of MDPI and/or the editor(s). MDPI and/or the editor(s) disclaim responsibility for any injury to people or property resulting from any ideas, methods, instructions or products referred to in the content.